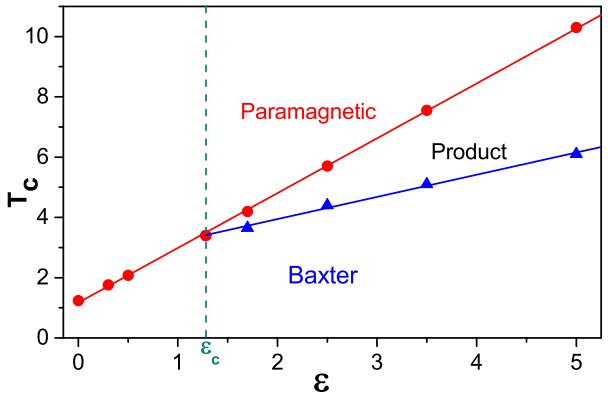

FIG. 1. (Color online) Phase diagram of the classical Hamiltonian (4) for $N = 3$ colors and disorder distribution (5) with $J_h = 1$, $J_l = 0.25$, and $c = 0.5$. The dots and triangles mark the numerically determined transitions between the Baxter, product, and paramagnetic phases. The solid lines are guides to the eye only. The dashed line marks $\epsilon_c = 1.281$ [see Eq. (3)] which separates the weak and strong coupling regimes in the strong-disorder renormalization group calculations.

where $\langle \ldots \rangle$ denotes the thermodynamic (Monte Carlo) average and $[\ldots]_{\rm dis}$ is the disorder average. In addition, we also measure the product order parameter

$$p = \frac{1}{3LL_t} \sum_{\alpha<\beta} \left| \sum_{i,t} S^\alpha_{i,t} S^\beta_{i,t} \right| \ , \qquad (8)$$

the corresponding product susceptibility χ_p, and the product Binder cumulant g_p.

The phase diagram of the classical Hamiltonian (4) resulting from these simulations is shown in Fig. 1. In the weak-coupling regime, $\epsilon < \epsilon_c$, we find a direct transition between the magnetically ordered Baxter phase at low temperatures and the paramagnetic high-temperature phase. For strong coupling, $\epsilon > \epsilon_c$, these two phases are separated by a product phase. In the following, we study the critical behaviors of the transitions separating these phases in detail, and we compare them to the renormalization group predictions.

B. Weak coupling regime

In the weak-coupling regime, $\epsilon < \epsilon_c$, we perform simulations for coupling strengths $\epsilon = 0$, 0.3 and 0.5 employing the Wolff and Swendsen-Wang cluster algorithms as discussed above. Because the disorder breaks the symmetry between the space and (imaginary) time directions in the Hamiltonian (4), the finite-size scaling analysis of the data to find the critical exponents becomes more complicated. This is caused by the fact that the system sizes L and L_t in the space and time directions are expected to have different scaling behavior. Thus, the correct aspect ratios L_t/L of the samples to be used in the simulations are not known a priori.

To overcome this problem we follow the iterative method employed in Refs. 45–48 which is based on the Binder cumulant. As the renormalization group calculations predict infinite-randomness criticality with activated dynamical scaling, the scaling form of the Binder cumulant (which has scale dimension 0) reads

$$g_{\rm av}(r, L, L_t) = X_g(rL^{1/\nu}, \ln(L_t/L_t^0)/L^\psi) \ . \qquad (9)$$

Here $r = (T - Tc)/T_c$ denotes the distance from criticality, X_g is a scaling function, and ψ and ν refer to the tunneling and correlation length critical exponents. L_t^0 is a microscopic reference scale. (For conventional power-law scaling, the second argument of the scaling function would read L_t/L^z with z being the dynamical exponent.) For fixed L, $g_{\rm av}$ has a maximum as function of L_t at position $L_t^{\rm max}$ and value $g_{\rm av}^{\rm max}$. The position of the maximum yields the *optimal* sample shape for which the system sizes L and L_t behave as the correlation lengths ξ and ξ_t. At criticality L_t must thus behave as $\ln(L_t^{\rm max}/L_t^0) \sim L^\psi$, fixing the second argument of the scaling function X_g. Consequently, the peak value $g_{\rm av}^{\rm max}$ is independent of L at criticality, and the $g_{\rm av}$ vs. r curves of optimally shaped samples cross at $T = T_c$. Once the optimal sample shapes are found, finite-size scaling proceeds as usual.[49,50]

To test our simulation and data analysis technique, we first consider the case $\epsilon = 0$ for which the quantum Ashkin-Teller model reduces to three decoupled random transverse-field Ising chains whose quantum phase transition is well understood.[4] We perform simulations for sizes $L = 10$ to 50 and $L_t = 2$ to 20000 and find a critical temperature $T_c \approx 1.24$. At this temperature, we confirm the activated scaling (9) of the Binder cumulant with the expected value $\psi = 1/2$. We also confirm the scaling of the magnetization at T_c (for the optimally shaped samples), $m \sim L^{-\beta/\nu}$ with $\beta = 0.382$ and $\nu = 2$.

After this successful test, we now turn to the Ashkin-Teller model proper. We perform two sets of simulations: (i) $\epsilon = 0.5$ using system sizes $L = 10$ to 60, $L_t = 2$ to 60000 and (ii) $\epsilon = 0.3$ with system sizes $L = 10$ to 50, $L_t = 2$ to 40000. In each case, we start from a guess for the optimal shapes and find an approximate value of T_c from the crossing of the $g_{\rm av}$ vs. T curves for different L. We then find the maxima of the $g_{\rm av}$ vs. L_t curves at this temperature which yield improved optimal shapes. After iterating this procedure two or three times, we obtain T_c and the optimal shapes with reasonable precision.

Figure 2 shows the resulting Binder cumulant $g_{\rm av}$ for $\epsilon = 0.5$ as function of L_t for different L at the approximate critical temperature of $T_c = 2.08(5)$. As expected at T_c, the maxima $g_{\rm av}^{\rm max}$ of these curves are independent of L (the slightly lower values at the smallest L can be attributed to corrections to scaling). Moreover, the figure shows that the $g_{\rm av}$ vs. L_t domes rapidly become broader with increasing spatial size L, indicating non-power-law scaling. To analyze this quantitatively, we present a scaling plot of these data in Fig. 3. For conventional power-